

Ice-shelf collapse from subsurface warming as a trigger for Heinrich events

Shaun A. Marcott^{a,1}, Peter U. Clark^a, Laurie Padman^b, Gary P. Klinkhammer^c, Scott R. Springer^d, Zhengyu Liu^e, Bette L. Otto-Bliesner^f, Anders E. Carlson^{e,g}, Andy Ungerer^c, June Padman^c, Feng He^e, Jun Cheng^h, and Andreas Schmittner^c

^aDepartment of Geosciences, Oregon State University, Corvallis, OR 97331; ^bEarth and Space Research, 3350 SW Cascade Avenue, Corvallis, OR 97333; ^cCollege of Oceanic and Atmospheric Sciences, Oregon State University, Corvallis, OR 97331; ^dEarth and Space Research, 2101 Fourth Avenue, Suite 1310, Seattle, WA 98121; ^eCenter for Climatic Research and Department of Atmospheric and Oceanic Sciences, University of Wisconsin, Madison, WI 53706; ^fClimate and Global Dynamics Division, National Center for Atmospheric Research, Boulder, CO 80307; ^gDepartment of Geoscience, University of Wisconsin, Madison, WI 53706; and ^hKey Laboratory of Meteorological Disaster, Nanjing University of Information Science and Technology, Nanjing, 210044, China

Edited by Mark H. Thiemens, University of California San Diego, La Jolla, CA, and approved June 30, 2011 (received for review March 25, 2011)

Episodic iceberg-discharge events from the Hudson Strait Ice Stream (HSIS) of the Laurentide Ice Sheet, referred to as Heinrich events, are commonly attributed to internal ice-sheet instabilities, but their systematic occurrence at the culmination of a large reduction in the Atlantic meridional overturning circulation (AMOC) indicates a climate control. We report Mg/Ca data on benthic foraminifera from an intermediate-depth site in the northwest Atlantic and results from a climate-model simulation that reveal basin-wide subsurface warming at the same time as large reductions in the AMOC, with temperature increasing by approximately 2 °C over a 1–2 kyr interval prior to a Heinrich event. In simulations with an ocean model coupled to a thermodynamically active ice shelf, the increase in subsurface temperature increases basal melt rate under an ice shelf fronting the HSIS by a factor of approximately 6. By analogy with recent observations in Antarctica, the resulting ice-shelf loss and attendant HSIS acceleration would produce a Heinrich event.

paleoceanography | paleoclimatology | abrupt climate change

Heinrich events represent the episodic discharge of icebergs from the Hudson Strait Ice Stream (HSIS) of the Laurentide Ice Sheet to the North Atlantic Ocean during late-Pleistocene glaciations (1). Although commonly attributed to internal ice-sheet instabilities (2), their occurrence at the culmination of a large reduction in the Atlantic meridional ocean circulation (AMOC) suggests a possible trigger by climate (3, 4). Models suggest that ocean responses to an AMOC reduction might destabilize the HSIS grounding line and trigger Heinrich events either through dynamic and steric sea-level rise or warming of intermediate-depth (hereafter subsurface) waters causing destabilization of ice shelves and attendant HSIS surging (4–6). Grounding lines, however, are thought to be stable to the decimeter-scale sea-level rise associated with a reduced AMOC (7). Moreover, evidence for subsurface warming remains widely debated (8–10), and the relationship between ocean temperature and total ice-shelf mass loss from basal melting is sensitive to the geometry and ocean setting of the specific ice shelf being considered (11).

Our study is based on core EW9302-2JPC (1,251 m, 48°47.70' N, 45°05.09' W) which, according to climate-model simulations, is at a depth and latitude that is ideal for monitoring subsurface warming associated with a reduction in the AMOC (Fig. 1) (4, 12). Previous work on this core identified ice-rafted detrital carbonate layers that represent Heinrich events (Fig. 2A), with associated changes in benthic faunas and the $\delta^{18}\text{O}$ of their carbonate tests that suggested intrusions of a relatively warm water mass coincident with the events (8). However, because the temperature transfer function for the benthic faunas is unknown, and ice-volume and hydrographic changes can mask the temperature signal in the $\delta^{18}\text{O}$ of calcite, the inferred temperature changes remain poorly constrained.

To further evaluate variability in bottom water temperature (BWT) at this site, we measured Mg/Ca in benthic foraminiferal calcite associated with the four Heinrich events (H1, H3, H5a, and H6) for which sufficient numbers of foraminifera existed in this core. Considering analytical and calibration uncertainties, we calculate an error of 1.3 °C for our Mg/Ca-derived BWT reconstructions. Recent work suggests that the $[\text{CO}_3^{2-}]$ ion may also affect Mg/Ca in some benthic foraminifera at temperatures below approximately 3 °C, where the carbonate ion saturation ($\Delta[\text{CO}_3^{2-}]$) decreases rapidly, and at low saturation levels (13). We used CO2SYS (14) to calculate modern $\Delta[\text{CO}_3^{2-}]$ at our site based on values of temperature, pressure, salinity, total alkalinity, total CO_2 , phosphate, and silicate retrieved from the World Ocean Circulation Experiment (WOCE) database (15). The corresponding value (approximately 55 mol/kg) suggests that the site is very weakly affected by the $[\text{CO}_3^{2-}]$ effect today (13). During the last glacial period, the deep Atlantic Ocean was less saturated in $[\text{CO}_3^{2-}]$, decreasing by approximately 20 $\mu\text{mol/kg}$ due to the intrusion of cold, undersaturated Antarctic Bottom Water (16). At intermediate-water depths (1–2 km) such as for our site, however, the glacial North Atlantic was approximately 20–30 $\mu\text{mol/kg}$ higher in $[\text{CO}_3^{2-}]$ than present and Holocene values (16), suggesting that our measured Mg/Ca values were not influenced by past $\Delta[\text{CO}_3^{2-}]$.

Results

Two independent temperature proxies support our Mg/Ca-derived BWTs. First, our reconstructed BWT at approximately 19 ka of 0 ± 1.3 °C agrees at 1σ with a Last Glacial Maximum temperature of -1.2 ± 0.2 °C reconstructed from pore fluids at site 981 on the Feni Drift (2,184 m; 55°29'N, 14°39'W) (17). Second, the amplitude and structure of the BWT change during the last deglaciation is in excellent agreement with the temperature change derived from the ice-volume corrected $\delta^{18}\text{O}$ ($\delta^{18}\text{O}_{\text{IVC}}$) measured on benthic fauna from this core assuming a temperature-dependent fractionation of 0.25‰ °C⁻¹ for calcite (18) (*SI Text*) (Fig. 2B).

The Mg/Ca data from EW9302-2JPC identify several systematic BWT changes that occurred in association with each of the four Heinrich ice rafted debris layers for which we have sufficient data (Fig. 2B) (1). Temperatures gradually increased prior to the start of each Heinrich layer, with the start of the warming begin-

Author contributions: P.U.C. designed research; S.A.M., L.P., S.R.S., Z.L., and B.L.O.-B. performed research; S.A.M., P.U.C., L.P., G.P.K., A.E.C., A.U., J.P., F.H., J.C., and A.S. analyzed data; and S.A.M., P.U.C., and L.P. wrote the paper.

The authors declare no conflict of interest.

This article is a PNAS Direct Submission.

¹To whom correspondence should be addressed. E-mail: marcotts@geo.oregonstate.edu.

This article contains supporting information online at www.pnas.org/lookup/suppl/doi:10.1073/pnas.1104772108/-DCSupplemental.

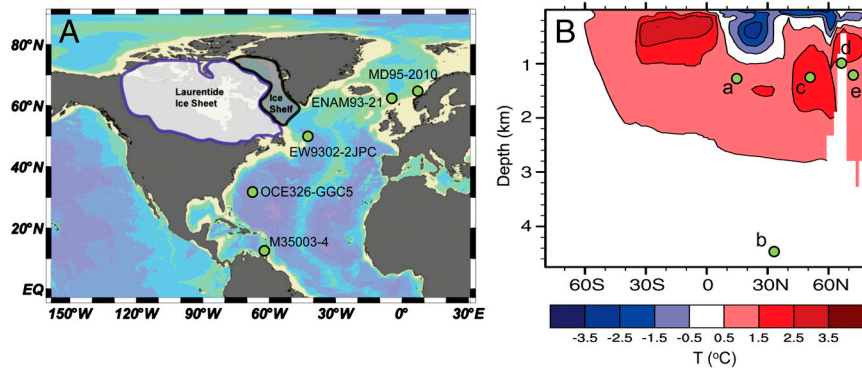


Fig. 1. (A) Location of core sites with records discussed in text (red dots). Also shown is extent of ice shelf derived from the Hudson Strait Ice Stream as reconstructed in ref. 31. (B) Zonal mean temperature anomaly in the Atlantic basin for a strongly reduced (approximately 4 Sv) versus active (approximately 13 Sv) AMOC (12). Location of core sites also shown: site a is core M35003-4, site b is core OCE326-GGC5, site c is core EW9302-2JPC, site d is core ENAM93-21, and site e is core MD95-2010.

ning approximately 1–2 kyr before each Heinrich event on our time scale. This early warming is replicated by the $\delta^{18}\text{O}_{\text{IVC}}$ (temperature) record associated with H1 (2). The warming trend prior to each Heinrich layer is consistently associated with a temperature oscillation of 3–4 °C (3). Each temperature oscillation occurs around a mean value that is close to the present BWT of approximately 3.4 °C and reaches a maximum BWT of 5–7 °C during the Heinrich layer.

A number of proxy records show that the AMOC began to decrease 1–2 kyr prior to Heinrich events (3, 19–22); this decline has been attributed to a climatically induced increase in freshwater fluxes from Northern Hemisphere ice sheets (4, 23). Model simulations indicate that, without an active AMOC and associated cooling of the ocean interior by convection, continued downward mixing of heat at low latitudes warms subsurface waters to a depth of approximately 2,500 m. Some of the heat accumulated in the subsurface is transported poleward, causing a temperature inversion in the northern North Atlantic (Fig. 1B) (4, 5, 12). We use results from a simulation with the National Center for Atmospheric Research Community Climate System Model version 3 (NCAR CCSM3) (12) to evaluate the transient response of the BWT at our core site to a reduction in the AMOC during the last deglaciation. Initial reduction in the AMOC occurs in response to increased freshwater fluxes to the North Atlantic associated with onset of deglaciation from the last glacial maximum at approximately 19 ka (Fig. 3A) (12, 23). Here we find that the simulated BWT anomaly at our core site caused by the change in the AMOC is in good agreement with our Mg/Ca-derived record, with temperature increasing by approximately 2 °C prior to H1, followed by cooling induced by the resumption of the AMOC at the start of the Bølling interstadial approximately 14.6 ka (Fig. 3C).

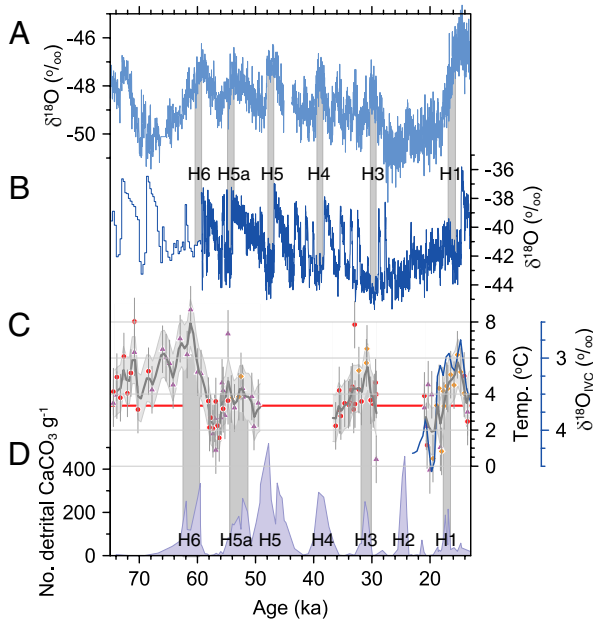


Fig. 2. (A) $\delta^{18}\text{O}$ record from Antarctic EPICA (European Project for Ice Coring in Antarctica) Dronning Maud Land ice core (37) on revised age model (38). (B) $\delta^{18}\text{O}$ record from the North Greenland Ice Core Project ice core (39) on revised age model (38) (<60 ka) and from Greenland Ice Core Project 2 ice core (>60 ka) on published age model (40). (C) Mg/Ca-derived bottom water temperatures for core EW9302-2JPC (1,251 m, 48°47.70'N, 45°05.09'W). Orange diamonds are measurements on *C. spp.*, purple triangles are on *C. lobulatus*, and red circles are on *M. barleeanum*. In order to filter the higher frequency signal to better evaluate the longer-term temperature changes, we linearly interpolated our data to a 10-yr interval and then applied a 500-yr Gaussian filter to derive the time series shown (thick gray line), with a 1.3 °C error based on analytical uncertainty. Also shown is the ice-volume corrected benthic $\delta^{18}\text{O}$ ($\delta^{18}\text{O}_{\text{IVC}}$) record from this core (blue line) during the last deglaciation (SI Text). (D) Number of ice-rafted detrital CaCO_3 grains g^{-1} of sediment in core EW9302-2JPC, with increases in these grains identifying Heinrich layers 1 through 6 (SI Text). Vertical gray bars represent timing of Heinrich events on the independent ice core (A and B) and EW9302-2JPC core (C and D) chronologies.

Although similar subsurface warming preceding H1 has been inferred in the subtropical (24) and high-latitude (25, 26) North Atlantic from changes in benthic foraminifera $\delta^{18}\text{O}$, the $\delta^{18}\text{O}$ changes in the Nordic Seas have alternatively been interpreted as recording increased brine formation beneath expanded sea ice (9, 10) and thus are largely independent of temperature. Our previously undescribed Mg/Ca measurements on *Cibicides spp.* ($N = 1$), *Cibicides lobulatus* ($N = 3$), and *Melonis barleeanum* ($N = 16$) for a core from the Nordic Seas (MD95-2010, 1,226-m depth) (Fig. 1B) demonstrate that the 1.5 per mil $\delta^{18}\text{O}_{\text{IVC}}$ signal at this site can be explained by approximately 6 °C of warming (Fig. 4A), thus supporting subsurface warming rather than brine formation as the cause of the large $\delta^{18}\text{O}_{\text{IVC}}$ signal. Changes in temperature simulated by the CCSM3 model further suggest that the $\delta^{18}\text{O}_{\text{IVC}}$ signal at this and other North Atlantic sites represents a dominant temperature control reflecting basin-wide subsurface warming (Fig. 4). The model also simulated small changes in salinity at intermediate depths as freshwater added to the surface was convected downward through the Labrador Sea in the subpolar gyre, suggesting that the associated advection of light $\delta^{18}\text{O}$ water may account for some small fraction of the $\delta^{18}\text{O}_{\text{IVC}}$ signal (Fig. 4) (SI Text).

Our Mg/Ca data also suggest a similar phasing between earlier changes in the AMOC, subsurface temperatures, and Heinrich events during marine isotope stage 3 (60–26 ka). In particular, correlation of marine records with synchronized Greenland

tion between ocean temperature T_i at the typical depth of the ice-shelf base (400–800 m), and shelf-averaged melt rate $M_{av} = 0.54 + 0.34.T_i$ (m a^{-1}). Based on the simulated temperature evolution for water depths of 400–800 m, our computed time history of ice-shelf thinning in response to the warming of intermediate-depth waters indicates an approximate 1,000-year time scale for collapse of the ice shelf (red curve in Fig. 3B), although based on modern analogs, it is likely that the ice shelf would collapse before it thinned to zero; we thus expect that our estimate of this time scale is a maximum. Additional factors (rate of grounding line migration and calving rate) may modulate this response, but are unlikely to significantly change the time scale (SI Text). The model also indicates that maximum melt rates along the deep grounding line of the HSIS increased sixfold, from approximately 6 m a^{-1} to $35\text{--}40 \text{ m a}^{-1}$, comparable to estimates from empirical models based on modern observations of grounding line melt rates (32). By analogy with recent studies of Antarctic ice shelves and buttressed ice streams (33), more rapid grounding line thinning would accelerate the HSIS outflow prior to ice-shelf collapse.

Conclusions

Our data and model results indicate that basin-wide subsurface warming occurred in the North Atlantic in response to a reduction in the AMOC prior to Heinrich events and that Heinrich events did not occur until the AMOC was at its weakest and subsurface temperatures were near their maximum values. We also find that the open-ocean subsurface warming significantly increases the rate of mass loss from the ice shelf fronting the HSIS. Our results thus support simplified climate modeling results, suggesting that a weakened or collapsed ice-shelf would trigger an ice-stream surge, producing a Heinrich event (5, 6), analogous to the recent response of Antarctic glaciers to the loss of buttressing ice shelves (34). By confirming the significance that

subsurface warming played in triggering past ice-sheet instabilities, our results provide important insights into possible future behavior of similarly configured Antarctic ice-sheet sectors, should warmer waters penetrate beneath their large, buttressing ice shelves.

Methods

We used an automated flow-through system (35) that cleans and dissolves the carbonate shells and thus minimizes the effects of secondary calcite and clay contamination (SI Text). We analyzed the benthic species *C. lobulatus* ($N = 46$), *C. spp.* ($N = 23$), and *M. barleeianum* ($N = 44$), including 15 replicate analyses, and converted Mg/Ca ratios to BWTs following published calibration curves (SI Text). The age model for EW9302-2JPC is based on six previously published ^{14}C dates (8), well-dated tephra layers at 16- (Vedde Ash) and 408-cm depth (ASH II), an age-to-depth tie point at the midpoint of H6 (36) corresponding to the peak in ice-rafted detrital carbonate at 496-cm depth in EW9302-2JPC, and the marine isotope stage 5/4 boundary (544 cm) based on the $\delta^{18}\text{O}$ planktonic foraminifera data from the core (8) (SI Text). We emphasize, however, that the relative timing of changes of any given proxy within the core relative to those of another proxy is established directly from the stratigraphic position of each sample within the core and is thus insensitive to any uncertainties in numerical chronology.

ACKNOWLEDGMENTS. We thank Ellen Roosen of the Woods Hole Oceanographic Institution core repository for subsampling of EW9302-2JPC, Trond Dokken (Bjerknes Center for Climate Research, Bergen, Norway) for providing samples from MD95-2010, Anne Jennings and Matthew Wolhowe for technical assistance, Tine Rasmussen for sharing data, and Thomas Bauska, Steven Hostetler, Alan Mix, Jeremy Shakun, Joseph Stoner, and two anonymous reviewers for comments. Support was provided by the National Science Foundation Paleoclimate Program (to P.U.C., G.P.K., A.E.C., Z.L., B.O.-B., and A.S.) and National Aeronautics and Space Administration Grant NNG05GR58G (to L.P.). Computer time was provided by the Department of Energy Innovative and Novel Computational Impact on Theory and Experiment program. This is Earth and Space Research contribution number 142.

- Heinrich H (1988) Origin and consequences of cyclic ice rafting in the Northeast Atlantic ocean during the past 130,000 years. *Quat Res* 29:142–152.
- MacAyeal DR (1993) Binge/purge oscillations of the Laurentide Ice Sheet as a cause of the North Atlantic's Heinrich events. *Paleoceanography* 8:775–784.
- Zahn R, et al. (1997) Thermohaline instability in the North Atlantic during meltwater events: Stable isotope and ice-rafted detritus records from core SO75-26KL, Portuguese margin. *Paleoceanography* 12:696–710.
- Clark PU, Hostetler SV, Piasias NG, Schmittner A, Meisner KJ (2007) Mechanisms for an ~7-kyrs climate and sea-level oscillation during Marine Isotope Stage 3. *Ocean Circulation: Mechanisms and Impacts—Past and Future Changes of Meridional Overturning*, eds A Schmittner, JCH Chiang, and SR Hemming (Am Geophysical Union, Washington, DC) p 392.
- Shaffer G, Olsen SM, Bjerrum CJ (2004) Ocean subsurface warming as a mechanism for coupling Dansgaard-Oeschger climate cycles and ice-rafting events. *Geophys Res Lett* 31:L24202, 10.1029/2004GL020968.
- Alvarez-Solas J, et al. (2010) Links between ocean temperature and iceberg discharge during Heinrich events. *Nat Geosci* 3:122–126.
- Alley RB, Anandakrishnan S, Dupont TK, Parizek BR, Pollard D (2007) Effect of sedimentation on ice-sheet grounding-line stability. *Science* 315:1838–1841.
- Rasmussen TL, Oppo DW, Thomsen E, Lehman SJ (2003) Deep sea records from the southeast Labrador Sea: Ocean circulation changes and ice-rafting events during the last 160,000 years. *Paleoceanography* 18, 10.1029/2001PA000736.
- Meland MY, Dokken TM, Jansen E, Hevrøy K (2008) Water mass properties and exchange between the Nordic seas and the northern North Atlantic during the period 23-6 ka: Benthic oxygen isotopic evidence. *Paleoceanography* 23:PA1210, 10.1029/2007PA001416.
- Dokken T, Jansen E (1999) Rapid changes in the mechanism of ocean convection during the last glacial period. *Nature* 401:458–461.
- Holland DM, Jenkins A (1999) Modelling thermodynamic ice-ocean interactions at the base of an ice shelf. *J Phys Oceanogr* 29:1787–1800.
- Liu Z, et al. (2009) Transient simulation of last deglaciation with a new mechanism for Bolling-Allerød warming. *Science* 325:310–314.
- Elderfield H, Yu J, Anand P, Kiefer K, Nyland B (2006) Calibrations for benthic foraminiferal Mg/Ca paleothermometry and the carbonate ion hypothesis. *Earth Planet Sci Lett* 250:633–649.
- Lewis E, Wallace DWR (1998) CO₂ system calculations, ORNU/CDIAC-105 (CO2SYS v.1.05).
- WOCE (2002) *World Ocean Circulation Experiment, Global Data, Version 30* (WOCE International Project Office, Southampton, UK).
- Yu J, Elderfield H, Pitrowski AM (2008) Seawater carbonate ion- $\delta^{13}\text{C}$ systematics and application to glacial-interglacial North Atlantic ocean circulation. *Earth Planet Sci Lett* 271:209–220.
- Adkins JF, McIntyre K, Schrag DP (2002) The salinity, temperature, and $\delta^{18}\text{O}$ of the glacial deep ocean. *Science* 298:1769–1773.
- O'Neil JR, Clayton RN, Mayeda TK (1969) Oxygen isotope fractionation in divalent metal carbonates. *J Chem Phys* 51:5547–5558.
- McManus JF, Francois R, Gherardi J-M, Keigwin LD, Brown-Leger S (2004) Collapse and rapid resumption of Atlantic meridional circulation linked to deglacial climate changes. *Nature* 428:834–837.
- Mangini A, et al. (2010) Deep sea corals off Brazil verify a poorly ventilated Southern Pacific Ocean during H2, H1 and the Younger Dryas. *Earth Planet Sci Lett* 293:269–276.
- Bond G, Lotti R (1995) Iceberg discharges into the North Atlantic on millennial time scales during the last deglaciation. *Science* 267:1005–1010.
- Gutjahr M, Hoogakker BAA, Frank M, McCave IN (2010) Changes in North Atlantic Deep Water strength and bottom water masses during Marine Isotope Stage 3 (45–35 ka BP). *Quat Sci Rev* 29:2451–2461.
- Clark PU, McCabe AM, Mix AC, Weaver AJ (2004) Rapid rise of sea level 19,000 years ago and its global implications. *Science* 304:1141–1144.
- Ruhlemann C, Mulitza S, Muller PJ, Wefer G, Zahn R (1999) Warming of the tropical Atlantic Ocean and slowdown of thermohaline circulation during the last deglaciation. *Nature* 402:511–514.
- Rasmussen TL, Thomsen E, van Weering TCE, Labeyrie L (1996) Rapid changes in surface and deep water conditions at the Faeroe Margin during the last 58,000 years. *Paleoceanography* 11:757–772.
- Rasmussen TL, Thomsen E (2004) The role of the North Atlantic Drift in the millennial timescale glacial climate fluctuations. *Paleogeogr Paleoclimatol Paleoecol* 210:101–116.
- Bond G, et al. (1993) Correlations between climate records from North Atlantic sediments and Greenland ice. *Nature* 365:143–147.
- Blunier T, Brook EJ (2001) Timing of millennial-scale climate change in Antarctica and Greenland during the last glacial period. *Science* 291:109–112.
- Rockey TJ (1992) North Atlantic deep water cools the southern hemisphere. *Paleoceanography* 7:489–497.
- Robinson LF, et al. (2005) Radiocarbon variability in the western North Atlantic during the last deglaciation. *Science* 310:1469–1473.
- Hulbe CL (1997) An ice shelf mechanism for Heinrich layer production. *Paleoceanography* 12:711–717.
- Rignot E, Jacobs SS (2002) Rapid bottom melting widespread near Antarctic Ice Sheet grounding lines. *Science* 296:2020–2023.

33. Joughin I, Smith BE, Holland DM (2010) Sensitivity of 21st century sea level to ocean-induced thinning of Pine Island Glacier, Antarctica. *Geophys Res Lett* 37:L20502, 10.1029/2010GL044819.
34. Rignot E, et al. (2004) Accelerated ice discharge from the Antarctic Peninsula following the collapse of Larsen B ice shelf. *Geophys Res Lett* 31:L18401, 10.1029/2004GL020697.
35. Haley BA, Klinkhammer GP (2002) Development of a flow-through system for cleaning and dissolving foraminiferal tests. *Chem Geol* 185:51–69.
36. Stoner JS, Channell JET, Hillaire-Marcel C, Kissel C (2000) Geomagnetic paleointensity and environmental record from Labrador Sea core MD95-2024: Global marine sediment and ice core chronostratigraphy for the last 110 kyr. *Earth Planet Sci Lett* 183:161–177.
37. Jouzel J, et al. (2007) Orbital and millennial Antarctic climate variability over the past 800,000 years. *Science* 317:793–796.
38. Lemieux-Dudon B, et al. (2010) Consistent dating for Antarctic and Greenland ice cores. *Quat Sci Rev* 29:8–20.
39. NGRIP members (2004) High-resolution record of Northern Hemisphere climate extending into the last interglacial period. *Nature* 431:147–151.
40. Meese DA (1997) The Greenland Ice Sheet Project 2 depth-age scale: Methods and results. *J Geophys Res* 102:26411–26423.
41. Rühlemann C, et al. (2004) Intermediate depth warming in the tropical Atlantic related to weakened thermohaline circulation: Combining paleoclimate data and modeling results for the last deglaciation. *Paleoceanography* 19, 10.1029/2003PA000948.

Supporting Information

Marcott et al. 10.1073/pnas.1104772108

SI Text

1. Mg/Ca Measurements. Only three species in our core have Mg/Ca temperature calibrations (*Melonis barleeanum*, *Cibicidoides lobatulus*, and *Cibicidoides spp.*), and these species only occurred in sufficient numbers for measurements to bracket the four Heinrich events H1, H3, H5a, H6. Moreover, because the species composition varies downcore, no one species was always available for each depth. At 15 depths, however, we replicated multispecies Mg/Ca measurements, of which 13 replicate at 1 σ and the other two replicate at 2 σ (Table S1). Mg/Ca ratios (mmol/mol) were converted to bottom water temperatures (BWTs) using calibrations developed in the North Atlantic Ocean near Iceland for *M. barleeanum* (1) [$\text{Mg/Ca} = 0.658 \times \exp(0.137 \times \text{BWT})$] and *C. lobatulus* (2) ($\text{Mg/Ca} = 1.10 + 0.129 \times \text{BWT}$). Mg/Ca ratios were converted to BWT for *C. spp.* [$\text{Mg/Ca} = 0.90 \times \exp(0.11 \times \text{BWT})$] using a global calibration (3). The automated flow-through system has an average standard deviation of 0.08 mmol/mol for duplicate Mg/Ca samples (4); combined with the temperature calibration error for the individual benthic species (1–3), the range of propagated uncertainty is 1.0–1.5 °C. Our Mg/Ca BWT error (approximately 1.3 °C) is in agreement with previous work where replicate foraminifera analysis, species calibration, and the carbonate ion ($[\text{CO}_3^{2-}]$) effect uncertainties are considered (1, 5, 6).

We measured 111 samples from core EW9302-2JPC and 20 samples from core MD95-2010 (Tables S1 and S2). We also made Mg/Ca measurements on two core-top samples, one on *C. spp.*, and one on *M. barleeanum*. Based on 17 hydrographic profiles within 50 km of our core, the range of BWT for depths 1,000–1,500 m is 3.29–3.86 (3.43 ± 0.28 at 2 σ) °C. Our core-top measurements are 4.9 ± 2.6 and 6.3 ± 2.6 °C (2 σ), which overlap at 2 σ . Based on the existing age model, however, it is unlikely that the core top is modern; extrapolating our age model from the two youngest age constraints [Vedde Ash (=12.2 ka) at 16 cm, calibrated ^{14}C age (=16.9 ka) at 32 cm] would suggest the core-top sample (1.5 cm) is approximately 7.5 ka.

2. Age Model. The age model for EW9302-2JPC is based on previously published ^{14}C dates, tephra layers at 16 cm (Vedde Ash) and 408-cm depth (ASH II), and tie points at 496 cm (peak of H6) to the age of peak of H6 determined by correlation to Greenland ice cores (7) and at 544-cm depth to the age of the marine isotope stage 5/4 boundary (8) (Table S1). The age model for MD95-2010 is based on previously published ^{14}C dates (9) that were recalibrated using Calib 6.0 (10) (Table S2).

3. Ice-Rafted Debris. Because the resolution (8 cm) of the original published detrital carbonate (DC) record from core EW9302-2JPC (8) is at a lower resolution than our temperature data, we generated new DC data for the Heinrich layers where we have temperature data from Mg/Ca. We duplicated the original counting protocols and then counted DC from several of the original intervals to demonstrate replication (Fig. S1).

4. Oxygen Isotopes. We made six new $\delta^{18}\text{O}$ measurements on *C. lobatulus*, *Cibicidoides wuellerstorfi* (each with 0.64 per mil correction for fractionation) and *M. barleeanum* (0.4 per mil correction) from core EW9302-2JPC at the Oregon State University (OSU) Stable Isotope Laboratory for the deglacial interval (20–13 ka) to supplement those already published (8). Prior to stable isotope measurements, benthic species were carefully selected so as to not incorporate “dirty” samples into the analysis.

Otherwise, all samples followed previous procedures (11). Sediment samples were cleaned and sieved with deionized water and calgon and dried at 40 °C. One to six specimens of *C. lobatulus*, *C. wuellerstorfi*, or *M. barleeanum* were used for each stable isotope measurement. All benthic foraminifera samples were sonicated in deionized water and methanol. Samples were then dried at room temperature (approximately 25 °C) for 24 h and then analyzed at OSU on a Finnigan-MAT 252 stable isotope ratio mass spectrometer equipped with a Kiel-III carbonate device. Samples were reacted at 70 °C in phosphoric acid, and all data are reported relative to the Pee Dee Belemnite standard through our internal standard, which is regularly calibrated against NBS-19.

We calculated the ice-volume corrected benthic $\delta^{18}\text{O}$ ($\delta^{18}\text{O}_{\text{IVC}}$) record for cores EW9302-2JPC and MD95-2010 during the last deglaciation where sufficient independent sea-level constraints exist. To calculate $\delta^{18}\text{O}_{\text{IVC}}$, we used a eustatic sea-level record (12) to subtract changes in seawater $\delta^{18}\text{O}$ from the published $\delta^{18}\text{O}$ record, assuming a relation of 1‰ change in seawater $\delta^{18}\text{O}$ is equivalent to 130-m sea level (13).

We calculated the change in intermediate water depth $\delta^{18}\text{O}$ due to the salinity decrease by assuming a meltwater end-member salinity of 0 psu and $\delta^{18}\text{O}$ of -25‰ to -35‰ (14, 15). We used the freshwater flux from Liu et al. (16) and solved for the ocean flux to match the change in salinity following Carlson (17). Substitution of the $\delta^{18}\text{O}$ end-member values (-25‰ to -35‰ for meltwater, $+1\text{‰}$ for ocean water) determines the change in $\delta^{18}\text{O}$. The modeled approximately 0.5-psu decrease in the Norwegian Sea equates to an approximate 0.4–0.5‰ decrease (-25‰ and -35‰ , respectively). The modeled approximately 0.3-psu decrease in the southeast Labrador Sea and in the Caribbean equates to an approximate 0.2–0.3‰ decrease (-25‰ and -35‰ , respectively).

5. Possible Contamination of Samples by Dolomite. Because Heinrich layers contain dolomite, negative $\delta^{18}\text{O}$ excursions in foraminifera associated with Heinrich layers may be due to contamination by fine dolomitic particles (18); similar contamination issues may apply to our Mg/Ca data. Because the flow-through method that we used for Mg/Ca measurements sequentially dissolves foram calcite from the surface inward, it allows us to evaluate any possible sources of contamination, which is its acknowledged strength in making Mg/Ca measurements. In particular, these data (Fig. S2) unequivocally demonstrate that there is no contamination of our forams by detrital dolomite, and thus this is not an issue for our $\delta^{18}\text{O}$ or Mg/Ca data. For example, Hodell and Curtiss (18) found increases in Ca/Sr associated with detrital carbonate in the Heinrich layers, suggesting that if our samples were contaminated by detrital carbonate, we should see increases in Ca/Sr of our forams. The absence of this signal thus demonstrates that there is no such contamination, indicating that it is not an issue for our $\delta^{18}\text{O}$ data. Similarly, the absence of a Mg signal in the outer part of our forams unequivocally demonstrates that there is no contamination of any surface coatings by dolomite, although we emphasize that the significance of the flow-through method is to remove any such coating on the shell before collecting data from the inner part of the foram shell, which we used in our study. Finally, we saw no evidence of dissolution of forams or lithic carbonate grains, indicating that there are no dissolution effects.

6. Ocean Model with Ice-Shelf Thermodynamic Coupling. The ocean model is based on the Regional Ocean Modeling System

(ROMS) version 3.0 (19, 20). ROMS is a free-surface, hydrostatic ocean model that solves the 3D primitive equations for a finite-difference lateral grid and a terrain-following vertical coordinate. For a recent application of ROMS with coupling to a thermodynamically active ice shelf, see Dinniman et al. (21).

The model was formulated on the domain shown in Fig. S3. The horizontal grid spacing is $\Delta x \approx 10$ km, and there are 25 vertical levels. Minimum thickness of the water column (ice base to seabed) is set to 200 m. Model bathymetry was based on TOPO12.1 (http://topex.ucsd.edu/marine_topo/mar_topo.html), an updated version of the global gridded bathymetry dataset first reported by Smith and Sandwell (22). The TOPO12.1 grid includes the International Bathymetric Chart of the Arctic Ocean (23).

The ice-shelf geometry follows Hulbe (24): The ice shelf fills Baffin Bay and grounds across Davis Strait, cutting off the northern portion of Baffin Bay, which is then excluded from our model. Ice draft (required for the model) is obtained from 0.85 times the modeled steady-state ice thickness in Hulbe (24).

The bathymetry grid was first smoothed to 10 km to match the final model grid spacing, then smoothed further to reduce errors that arise in the baroclinic pressure gradient calculation in models that use terrain-following vertical coordinate systems (25). See Padman et al. (26) for details on numerical requirements for smoothing and smoothing methodology. The ice-shelf draft fields digitized from Hulbe (24) were already sufficiently smooth.

Model hydrography is derived from a simulation with the National Center for Atmospheric Research Community Climate System Model version 3 (NCAR CCSM3) (16). As initial conditions we use profiles, averaged over 500 y, taken from near the center of the ice-shelf front (Fig. S4), and assume horizontal homogeneity. We ran five states: a “cold” state (model years 19.5–19.0 ka), three intermediate states (18.5–18.0 ka, 18.0–17.5 ka, and 17.5–17.0 ka) and a “warm” state (17.0–16.5 ka). The approximate values of subsurface temperature from CCSM3 for these five periods each averaged over the 400- to 800-m depth range corresponding to ice-shelf draft, are $T_i = -1.1^\circ\text{C}$, -1.1°C , -0.8°C , $+0.6^\circ\text{C}$, and $+1.7^\circ\text{C}$, respectively.

The model was forced by barotropic tides (tide height and currents) at the open boundaries. Tides were recalculated for a larger-domain model of the North Atlantic Ocean, using open boundary conditions from the modern global barotropic tide model TPX07.2 (27). Geometry in the Labrador Sea and Baffin Bay was modified to reflect the presence of the specified ice shelf. We assume that the effect of tides of the change in geometry due to the ice shelf does not extend to the boundaries of the larger-domain model. The addition of tides to the circulation that would develop independently through buoyancy fluxes at the ice-shelf base speeds up model equilibration but, for this case, has little effect on the steady-state basal melt rate distribution.

We use the three-equation formulation of ice/ocean thermodynamic exchange described by Holland and Jenkins (28) as applied in ROMS by Dinniman et al. (21). In our application, the friction velocity is calculated at each time step, and so explicitly includes

the effects of time-varying tidal currents as well as the thermohaline circulation, or “plume flow,” associated with basal melt.

Vertical mixing elsewhere in the model was parameterized by the Mellor–Yamada level 2.5 turbulence closure scheme (29). Benthic stress was modeled as quadratic drag with $c_d = 0.003$. We used a Laplacian (“harmonic”) formulation for the horizontal mixing of momentum and tracers, with coefficients of the lateral viscosity A_H and diffusivity K_H both set to $5\text{ m}^2\text{ s}^{-1}$.

Maps of predicted basal melt rate M_b (Fig. S4) for the cold (19.5–19 ka) and warm (17–16.5 ka) states show similar structure, with highest rates along southwest Greenland where the inflowing water first meets deeply grounded ice and at the deep grounding line of the Hudson Strait Ice Stream (HSIS). However, the magnitude of M_b for the warm state is about six times higher than for the cold state so that the difference map $\Delta M_b = M_b(\text{warm}) - M_b(\text{cold})$ (Figure S5, *Right*) looks similar to $M_b(\text{warm})$.

Modern ice shelves tend to lose approximately 1/2 of their mass through basal melting and 1/2 through calving. The Hulbe model (24) assumed that, at steady state, ice-volume input across the HSIS grounding line (approximately $660\text{ km}^3\text{ a}^{-1}$) was balanced entirely by calving at a specified ice front (Fig. S3). The shelf-integrated mass loss due to modeled mean basal melt (approximately 0.17 ma^{-1}) in the cold state corresponds to approximately $70\text{ km}^3\text{ a}^{-1}$, or approximately 10% of the total mass loss.

The linear relationship between ice-front CCSM3 temperature T_i and shelf-averaged basal melt rate M_{av} from our five simulations is

$$M_{\text{av}} = 0.54 + 0.34.T_i(\text{ma}^{-1}).$$

From this equation and the time series of T_i at the original temporal resolution of the model output (10 y), we estimate a time history of shelf-integrated mass loss corresponding to the excess melt rate relative to the cold-state value (assumed to represent a steady-state ice shelf). Mass loss begins near 18 ka. Integration of this mass loss in time leads to total removal of the ice shelf near 16.7 ka.

This estimate of collapse time requires several assumptions: (i) calving rate remains constant throughout the transition to the warm state, (ii) the HSIS ice-volume flux remains constant even as the ice shelf thins, (iii) the area-averaged basal melt rate follows the above linear relationship to T_i even as the ice-shelf draft decreases by excess melt, (iv) the opening of northern Baffin Bay (north of Davis Strait) as the ice shelf thins has no impact on subsequent circulation or melt rate of the modeled portion of the ice shelf, and (v) net surface accumulation of mass (snow-fall) directly on the ice shelf is an insignificant term in the ice-shelf mass budget under all experienced climate states, or can be incorporated as a revision to the calving flux of approximately $590\text{ km}^3\text{ a}^{-1}$. Violation of any of these assumptions will change the integrated mass loss and collapse time in ways that cannot be quantified without fully coupled ocean, glaciological, and atmospheric models.

- Kristj nsd ttir GB, Lea DW, Jennings AE, Pak DK, Belanger CL (2007) New spatial Mg/Ca-temperature calibrations for three Arctic, benthic foraminifera and reconstruction of north Iceland shelf temperature for the past 4000 years. *Geochem Geophys Geosys* 8:Q03P21 (10.1029/2006GC001425).
- Quillman U, Marchitto TM, Andrews JT, Jennings AE, Dean WE (2008) 38th International Arctic Workshop, Abstracts and Programs.
- Elderfield H, Yu J, Anand P, Kiefer T, Nyland B (2006) Calibrations for benthic foraminiferal Mg/Ca paleothermometry and the carbonate ion hypothesis. *Earth Planet Sci Lett* 250:633–649.
- Klinkhammer GP, Haley BA, Mix AC, Benway HM, Cheseby M (2004) Evaluation of automated flow-through time-resolved analysis of foraminifera for Mg/Ca paleothermometry. *Paleoceanography* 19:PA4030 (10.1029/2004PA001050).
- Lear CH, Rosenthal Y, Slowey N (2002) Benthic foraminifera Mg/Ca-paleothermometry: A revised core-top calibration. *Geochim Cosmochim Acta* 66:3375–3387.
- Sosdian S, Rosenthal Y (2009) Deep-sea temperature and ice volume changes across the Pliocene-Pleistocene climate transition. *Science* 325:306–310.
- Stoner JS, Channell JET, Hillaire-Marcel C, Kissel C (2000) Geomagnetic paleointensity and environmental record from Labrador Sea core MD95-2024: Global marine sediment and ice core chronostratigraphy for the last 110 kyr. *Earth Planet Sci Lett* 183:161–177.
- Rasmussen TL, Oppo DW, Thomsen E, Lehman SJ (2003) Deep sea records from the southeast Labrador Sea: Ocean circulation changes and ice-rafting events during the last 160,000 years. *Paleoceanography* 18 (10.1029/2001PA000736).
- Dokken T, Jansen E (1999) Rapid changes in the mechanism of ocean convection during the last glacial period. *Nature* 401:458–461.
- Hughen KA, et al. (2004) Marine04 marine radiocarbon age calibration, 0–26 cal kyr BP. *Radiocarbon* 46:1059–1086.
- Benway HM, Mix AC, Haley BA, Klinkhammer GP (2006) Eastern Pacific Warm Pool paleosalinity and climate variability: 0–30 kyr. *Paleoceanography* 21:PA3008, 10.1029/2005PA001208.
- Bassett SE, Milne GA, Mitrovica JX, Clark PU (2005) Ice sheet and solid earth influences on far-field sea-level histories. *Science* 309:925–928.

Table S1. Mg/Ca data for core EW9302-2JPC

Depth, cm				
Midpoint	Age, y	Mg/Ca	BWT, °C	Species
1.5	0	1.798	6.2912	<i>C. spp.</i>
1.5	0	1.283	4.8741	<i>M. barl.</i>
12.5	11,208	1.321	3.4886	<i>C. spp.</i>
18.5	12,954	1.556	4.9771	<i>C. spp.</i>
20.5	13,536	1.491	3.0058	<i>C. lobt.</i>
20.5	13,536	0.924	2.4782	<i>M. barl.</i>
22.5	14,118	1.403	4.0361	<i>C. spp.</i>
22.5	14,118	1.306	5.0038	<i>M. barl.</i>
24.5	14,700	1.599	5.2249	<i>C. spp.</i>
26.5	15,282	1.776	6.1793	<i>C. spp.</i>
28.5	15,864	1.476	4.4972	<i>C. spp.</i>
30.5	16,446	1.573	5.0759	<i>C. spp.</i>
32.5	16,935	1.446	4.3106	<i>C. spp.</i>
34.5	17,148	1.467	4.4416	<i>C. spp.</i>
38.5	17,573	1.299	3.336	<i>C. spp.</i>
40.5	17,786	1.427	4.1903	<i>C. spp.</i>
42.5	17,999	0.985	0.8204	<i>C. spp.</i>
44.5	18,212	1.238	1.0453	<i>C. lobt.</i>
46.5	18,424	1.447	4.3168	<i>C. spp.</i>
50.5	18,850	1.303	3.3639	<i>C. spp.</i>
56.5	19,488	0.943	0.4243	<i>C. spp.</i>
58.5	19,701	1.611	3.9612	<i>C. lobt.</i>
61.5	20,020	1.073	-0.2093	<i>C. lobt.</i>
64.5	20,309	1.683	4.5194	<i>C. lobt.</i>
68.5	20,494	0.772	1.1663	<i>M. barl.</i>
71.5	20,632	1.385	2.2093	<i>C. lobt.</i>
78.5	20,955	1.518	3.2403	<i>C. lobt.</i>
78.5	20,955	1.123	3.9019	<i>M. barl.</i>
203.5	29,245	1.149	0.3798	<i>C. lobt.</i>
203.5	29,245	1.135	3.9794	<i>M. barl.</i>
205.5	29,351	1.241	4.6312	<i>M. barl.</i>
209.5	29,563	1.109	3.8103	<i>M. barl.</i>
213.5	29,775	1.056	3.4528	<i>M. barl.</i>
221.5	30,199	1.086	3.6573	<i>M. barl.</i>
233.5	30,835	1.842	6.511	<i>C. spp.</i>
235.5	30,941	1.69	5.7281	<i>C. spp.</i>
245.5	31,789	1.076	3.5898	<i>M. barl.</i>
249.5	32,232	1.613	5.3041	<i>C. spp.</i>
249.5	32,232	1.179	4.2571	<i>M. barl.</i>
255.5	32,897	1.055	3.4459	<i>M. barl.</i>
256	32,952	1.93	7.8545	<i>M. barl.</i>
257.5	33,118	1.013	3.1494	<i>M. barl.</i>
259.5	33,340	1.203	4.4042	<i>M. barl.</i>
261.5	33,561	1.175	4.2323	<i>M. barl.</i>
263.5	33,783	1.065	3.5148	<i>M. barl.</i>
265.5	34,004	1.05	3.4112	<i>M. barl.</i>
271.5	34,669	1.061	3.4873	<i>M. barl.</i>
277.5	35,333	0.963	2.7799	<i>M. barl.</i>
279.5	35,555	1.009	3.1205	<i>M. barl.</i>
280	35,610	1.17	4.2011	<i>M. barl.</i>
285.5	36,219	0.894	2.2372	<i>M. barl.</i>
325.5	40,649	1.89	6.0976	<i>C. lobt.</i>
327.5	40,871	1.194	0.7044	<i>C. lobt.</i>
328	40,926	1.36	1.9907	<i>C. lobt.</i>
335.5	41,757	1.258	1.2003	<i>C. lobt.</i>
351.5	44,694	1.462	2.7811	<i>C. lobt.</i>
357.5	45,810	1.951	7.0337	<i>C. spp.</i>
359.5	46,182	1.503	3.0988	<i>C. lobt.</i>
363.5	46,925	1.339	1.828	<i>C. lobt.</i>
377.5	49,529	1.555	3.5017	<i>C. lobt.</i>
381.5	50,272	1.387	2.1999	<i>C. lobt.</i>
383.5	50,644	1.602	3.8659	<i>C. lobt.</i>
391.5	52,132	1.598	3.8349	<i>C. lobt.</i>
392	52,225	1.66	4.3154	<i>C. lobt.</i>
393.5	52,504	1.557	4.9829	<i>C. spp.</i>
395.5	52,876	1.375	3.8529	<i>C. spp.</i>
399.5	53,619	1.521	3.2383	<i>C. lobt.</i>
402.5	54,177	1.356	3.7264	<i>C. spp.</i>

Table S2. Data for core MD95-2010

Depth, cm					
Midpoint	Age, y	Mg/Ca	Species	BWT, °C	Notes
54.5	12,549	—	—	—	calibrated ¹⁴ C age
123.5	14,236	1.22	<i>M. barl.</i>	4.505	
129.5	14,382	1.549	<i>M. barl.</i>	6.249	
133.5	14,479	1.128	<i>M. barl.</i>	3.934	
134.5	14,504	1.149	<i>M. barl.</i>	4.069	
134.5	14,504	1.62	<i>C. lobt.</i>	4.031	
136.5	14,540	—	—	—	calibrated ¹⁴ C age
146.5	15,242	1.96	<i>C. spp.</i>	7.075	
156.5	15,911	2.758	<i>C. lobt.</i>	12.853	
159	16,079	2.828	<i>M. barl.</i>	10.643	sample interval: 158–160 cm
161.5	16,246	2.95	<i>C. lobt.</i>	14.341	
173.5	17,015	—	—	—	calibrated ¹⁴ C age
192.5	17,841	2.457	<i>M. barl.</i>	9.617	
197.5	18,032	—	—	—	calibrated ¹⁴ C age
199.5	18,063	1.726	<i>M. barl.</i>	7.039	
202.5	18,100	1.684	<i>M. barl.</i>	6.859	
204.5	18,125	1.54	<i>M. barl.</i>	6.207	
206.5	18,150	1.557	<i>M. barl.</i>	6.287	
209	18,181	1.535	<i>M. barl.</i>	6.183	sample interval: 208–210 cm
213	18,231	1.787	<i>M. barl.</i>	7.293	sample interval: 212–214 cm
226.5	18,399	3.673	<i>C. lobt.</i>	—	suspect value; not included
227	18,405	1.922	<i>M. barl.</i>	7.824	sample interval: 226–228 cm
233	18,479	1.419	<i>M. barl.</i>	5.61	sample interval: 232–234 cm
246	18,641	1.814	<i>M. barl.</i>	7.402	sample interval: 245–247 cm
251	18,703	1.725	<i>M. barl.</i>	7.035	sample interval: 250–252 cm
300.5	19,312	—	—	—	calibrated ¹⁴ C age

Subsampling for Mg/Ca measurements was done in centimeter intervals except where indicated.

Table S3. Age-depth data for EW9302-2JPC

Depth, cm	¹⁴ C Age, y	Error, 1σ	Calibrated ¹⁴ C Age, y	Error	Notes
16	10,300	100	12,226	257	Vedde Ash
32	13,770	130	16,882	125	
64	17,090	120	20,286	161	
161	20,780	150	24,760	205	
200	24,280	240	29,059	306	
240	26,710	240	31,180	123	
336	36,950	700	41,812	505	
408	—	—	55,200	—	Ash II
496	—	—	59,500	—	H6 Tie Point
544	—	—	74,000	—	Stage 5/4